AGU PUBLICATIONS

JGR

Journal of Geophysical Research: Earth Surface

RESEARCH ARTICLE

10.1002/2015JF003600

Illuminating wildfire erosion and deposition patterns with repeat terrestrial lidar

F. K. Rengers[1,2], G. E. Tucker[1], J. A. Moody[3], and B. A. Ebel[4]

[1]CIRES and Department of Geological Sciences, University of Colorado Boulder, Boulder, Colorado, USA, [2]U.S. Geological Survey Geological Hazards Science Center, Golden, Colorado, USA, [3]U.S. Geological Survey National Research Program, Boulder, Colorado, USA, [4]U.S. Geological Survey National Research Program, Lakewood, Colorado, USA

Key Points:
- Post-fire erosion is spatially variable
- Hillslopes generate more erosion than channels at our site
- Post-wildfire erosion patterns evolve due to changing roughness

Supporting Information:
- Tables S1 and S2 and Figures S1–S15

Correspondence to:
F. K. Rengers,
frengers@usgs.gov

Citation:
Rengers, F. K., G. E. Tucker, J. A. Moody, and B. A. Ebel (2016), Illuminating wildfire erosion and deposition patterns with repeat terrestrial lidar, *J. Geophys. Res. Earth Surf.*, *121*, 588–608, doi:10.1002/2015JF003600.

Received 28 APR 2015
Accepted 13 FEB 2016
Accepted article online 18 FEB 2016
Published online 11 MAR 2016

Abstract Erosion following a wildfire is much greater than background erosion in forests because of wildfire-induced changes to soil erodibility and water infiltration. While many previous studies have documented post-wildfire erosion with point and small plot-scale measurements, the spatial distribution of post-fire erosion patterns at the watershed scale remains largely unexplored. In this study lidar surveys were collected periodically in a small, first-order drainage basin over a period of 2 years following a wildfire. The study site was relatively steep with slopes ranging from 17° to > 30°. During the study period, several different types of rain storms occurred on the site including low-intensity frontal storms (2.4 mm h^{-1}) and high-intensity convective thunderstorms (79 mm h^{-1}). These storms were the dominant drivers of erosion. Erosion resulting from dry ravel and debris flows was notably absent at the site. Successive lidar surveys were subtracted from one another to obtain digital maps of topographic change between surveys. The results show an evolution in geomorphic response, such that the erosional response after rain storms was strongly influenced by the previous erosional events and pre-fire site morphology. Hillslope and channel roughness increased over time, and the watershed armored as coarse cobbles and boulders were exposed. The erosional response was spatially nonuniform; shallow erosion from hillslopes (87% of the study area) contributed 3 times more sediment volume than erosion from convergent areas (13% of the study area). However, the total normalized erosion depth (volume/area) was highest in convergent areas. From a detailed understanding of the spatial locations of erosion, we made inferences regarding the processes driving erosion. It appears that hillslope erosion is controlled by rain splash (for detachment) and overland flow (for transport and quasi-channelized erosion), with the sites of highest erosion corresponding to locations with the lowest roughness. By contrast, in convergent areas we found erosion caused by overland flow. Soil erosion was locally interrupted by immobile objects such as boulders, bedrock, or tree trunks, resulting in a patchy erosion network with increasing roughness over time.

1. Introduction

Post-wildfire erosion is typically much greater than erosion in unburned forests due to the hydrologic, ecologic, and pedologic disturbances that accompany wildfire [*Sinclair and Hamilton*, 1955; *Imeson et al.*, 1992; *Benavides-Solorio and MacDonald*, 2001; *Istanbulluoglu et al.*, 2003, 2004; *Moody et al.*, 2005; *Shakesby and Doerr*, 2006; *Sheridan et al.*, 2007; *Robichaud et al.*, 2010]. Wildfire heating can alter soil erodibility [*Moody et al.*, 2005] by destroying organic matter [*Stoof et al.*, 2010] such as plant tissue, roots, and soil microorganisms, which all play a part in soil cohesion and structure [*Hungerford et al.*, 1991; *Busse et al.*, 2010; *Chief et al.*, 2012]. Combustion of vegetation can reduce vegetation roughness increasing debris flow susceptibility [e.g., *Istanbulluoglu et al.*, 2004] and releasing colluvium previously trapped by vegetation on hillslopes [*DiBiase and Lamb*, 2013]. The decay of burned plant roots can decrease soil shear strength [*Schmidt et al.*, 2011] and encourage landsliding [*Gabet and Mudd*, 2006; *Jackson and Roering*, 2009]. Increases in bare soil after a fire can augment the erosional effects of rain splash detachment [*Shakesby et al.*, 1993; *Gabet and Dunne*, 2003], overland flow, and rain flow, a combination of rain splash detachment and overland flow transport [*Moss*, 1988]. Finally, increased runoff due to post-fire hydrophobicity [*DeBano*, 2000; *Doerr et al.*, 2000; *Robichaud and Hungerford*, 2000; *Moody and Ebel*, 2012] can increase interrill erosion [*Sheridan et al.*, 2007], rill erosion [*Robichaud et al.*, 2010], and debris flow erosion [*Cannon et al.*, 2003; *Gabet*, 2003a; *Istanbulluoglu et al.*, 2003, 2004; *Nyman et al.*, 2011].

©2016. American Geophysical Union. All Rights Reserved.

The magnitude and duration of increased erosion following wildfire can vary markedly in different settings [*Shakesby and Doerr*, 2006]. In order to understand the factors responsible for these variations, and ultimately perhaps predict them, it is necessary to understand the mechanisms at play. This requires knowledge of the spatial patterns of erosion. For example, sediment might derive mainly from erosional "hot spots" such as low-order channels and other topographically convergent areas where runoff tends to concentrate, or it might originate from broadly distributed overland flow erosion on hillslopes that constitute the majority of a catchment's surface area.

Much previous research has been done to measure erosion after wildfires [*Moody and Martin*, 2001a; *Benavides-Solorio and MacDonald*, 2005; *Shakesby and Doerr*, 2006]. These methods typically involve collecting sediment eroded from a known contributing area (using silt fences or reservoirs as traps) or point measurements (using erosion pins, cross-sectional change, and radionuclide depletion) [*Moody et al.*, 2008]. While these techniques show the integrated change over an area, none of these conventional methods reveal the spatial distribution of erosion at the scale of erosional change (1 – 10 cm).

Those few studies that have focused on pinpointing sediment sources have shown that erosional patterns vary from case to case. For example, using fallout radionuclide measurements, *Owens et al.* [2012] found that the majority of post-fire sediment erosion originated from channelized areas, with a much smaller contribution from hillslopes. A similar observation was made by *Moody and Martin* [2001a]. Other researchers have documented an opposite finding, with distributed hillslope erosion contributing more sediment than channelized erosion [*Wilkinson et al.*, 2009; *Smith et al.*, 2011]. These diverse findings highlight the need for new and more efficient methods to document the spatial distribution of post-wildfire erosion.

Terrestrial laser scanning (TLS) is a useful technology for rapid, detailed measurement of erosion/deposition patterns [*Collins and Sitar*, 2008; *Wheaton et al.*, 2010; *Day et al.*, 2012; *Lague et al.*, 2013] and changes in surface roughness [*Sankey et al.*, 2011; *Lague et al.*, 2013]. Because the data acquisition process is relatively efficient, noninvasive [*Collins et al.*, 2012], and suitable for steep terrain [*Staley et al.*, 2014]; repeat surveys over a period of weeks to years make it possible to detect centimeter-scale changes in topography over time [*Wheaton et al.*, 2010; *Schmidt et al.*, 2011; *Soulard et al.*, 2013; *Staley et al.*, 2014]. Studies in the steep shrublands of the San Gabriel mountains, California, have demonstrated the potential of TLS to quantify post-fire morphologic change [*Schmidt et al.*, 2011; *Staley et al.*, 2014]. Additionally, *Gupta et al.* [2015] have shown the utility of using TLS to quantify biomass changes in burned forests. However, steep, heavily forested environments also present challenges because burned sites typically contain numerous standing tree trunks that generate shadows in TLS surveys [*DeLong et al.*, 2012; *Orem and Pelletier*, 2015].

This paper describes the use of multitemporal TLS to quantify post-wildfire erosion in a forested, lower montane environment. Five lidar surveys were conducted over a period of 20 months at a study site in the Colorado Front Range that was severely burned during the 2010 Fourmile Canyon fire. Erosion and deposition were monitored using the morphological method, whereby repeat measurements of topography substitute for the direct measurement of sediment flux [*Brasington et al.*, 2000]. TLS was also used to quantify morphometric attributes such as roughness, which is typically difficult to measure over large areas.

In addition to detailed topography from TLS, soil properties such as erodibility and soil bulk density were measured at the site [*Moody and Nyman*, 2013]. This provides insight into the site erosional response and allows us to convert changes in topographic volume to the mass of erosion between surveys. Rainfall and runoff were also measured for each storm to relate erosional change to hydrologic drivers. The monitoring period included frontal storms and convective storms, which allowed for observations of erosional response from different rainstorm types.

With this unique data set of topography, soil properties, and hydrology, we monitored erosional patterns in distinctive morphologic units on the study site. The data were used to explore several research questions. How do post-fire erosion patterns and magnitude evolve over time? How does the erosional response after a wildfire relate to intrinsic (e.g., slope and local geomorphology) and extrinsic (e.g., rainfall) variables? Overall, the results demonstrate that it is possible to answer these questions and to document the geomorphic legacy of wildfire, through the use of repeat terrestrial lidar surveys.

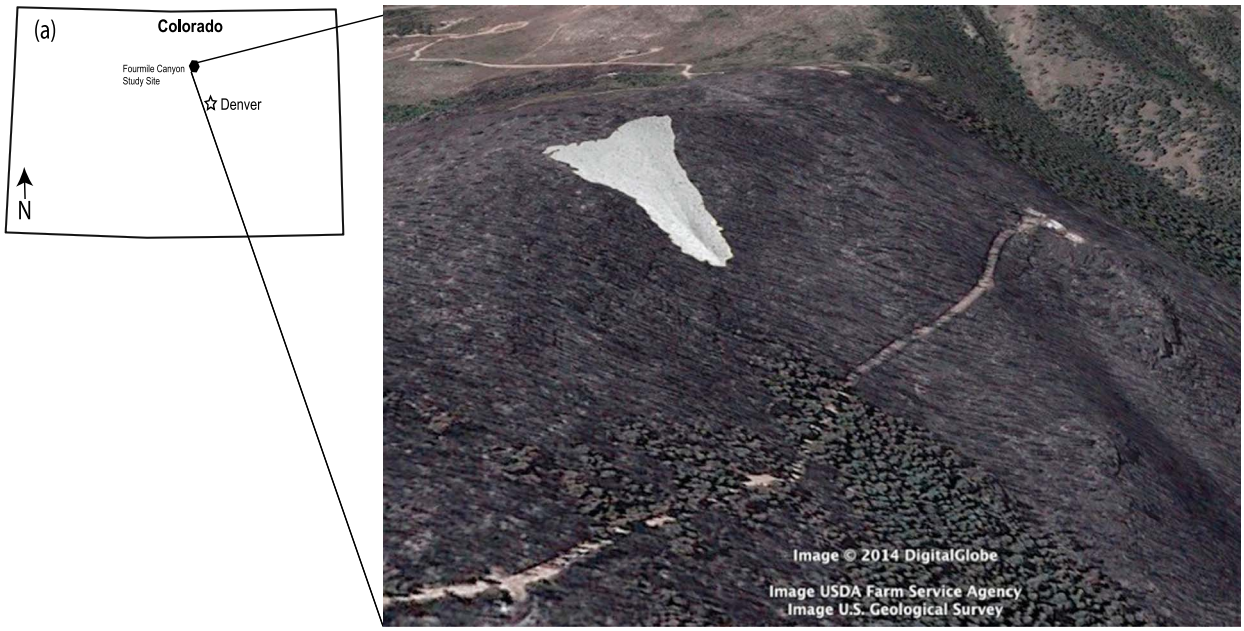

Figure 1. (a) Site location in Colorado, USA. (b) Oblique view of study site, with gray-shaded relief polygon delineating the study area.

2. Study Site

The study site is located in the foothills of the Colorado Front Range, approximately 12 km west of Boulder, Colorado, and was burned in the Fourmile Canyon Fire (6–13 September 2010). The site is a mesic first-order drainage basin (contributing area of 5500 m^2) that transitions from a ridge top to a concave hillslope with a colluvial channel (using the channel definition of *Montgomery and Buffington* [1997]) (Figures 1 and 2). This location was chosen because it falls within a high burn severity zone.

The site is underlain by the Boulder Creek granodiorite, and prior to the wildfire it was forested with a Rocky Mountain subspecies of Douglas fir (*Pseudotsuga menziesii* subspecies *glauca*), limber pine (*Pinus flexilis*), and aspen (*Populus tremuloides*) [*Ebel et al.*, 2012a]. The mean annual precipitation (500 mm) falls in three distinct precipitation regimes: snowfall in the winter (November–March), cyclonic rain storms (April–May and September–October), and monsoonal convective rain storms (July–August) [*Ebel et al.*, 2012a]. Snowmelt contributes 60–75% of the water flux to the subsurface, and the snowpack at the study location typically lasts weeks to months [*Ebel et al.*, 2012b].

Soil at the field site is colluvium/residuum derived from the granodiorite bedrock, which forms a gravelly sandy loam (part of the Allen's Park Member of the Fern Cliff-Allens Park-Rock outcrop complex) [*Moreland and Moreland*, 1975]. The soils are formally classified as frigid Lamellic Haplustalfs and frigid Typic Haplustalfs [*Ebel et al.*, 2012a]. The texture is coarsest in the surface layer (0–0.5 cm) with 17–33% gravel (2–32 mm), 50–71% sand (0.063–2 mm), and 9–18% silt and clay (<0.063 mm) [*Moody and Nyman*, 2013, Table 2]. During qualitative field observations at the beginning of the study, few particles greater than 64 mm were visible on the site. This distribution changed over the study period after many boulders were exposed via erosion.

Immediately after the fire, the soil was covered by a layer of ash, which profoundly influences post-wildfire hydrology [*Ebel et al.*, 2012a]. An ash survey (conducted between the first two TLS surveys) showed that the mean ash depth was 1.8 cm, with minimum and maximum values of 0.1 cm and 8.0 cm, respectively [*Ebel et al.*, 2012a].

3. Methods

3.1. TLS Methods

The morphological method was employed at the study site using five terrestrial lidar surveys over a period of 2 years (Table 1). The first survey was undertaken 24 days after the wildfire was contained and prior to any rainfall. The second survey was conducted 11 days later (following a rainstorm), and these two surveys covered the entire study area (see shaded relief in Figure 2). A survey on 12 July 2011 obtained data from half

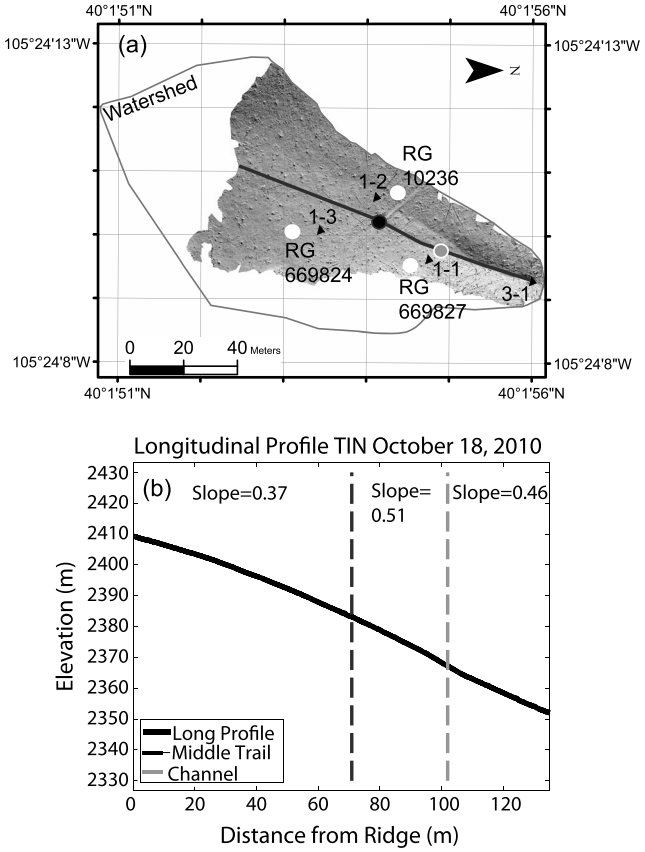

Figure 2. (a) Shaded relief map of the terrestrial lidar data with watershed outline (grey line). Downhill is in the north direction. The black point represents an east-west trending trail "middle trail" across the site. The gray point inside a white ring represents where channelization begins. Rain gages (RG) are the white circles, and flumes are the black triangles. The black line shows the location of the longitudinal profile in Figure 2b. (b) Longitudinal profile, where the average slope is labeled for three zones. The black and gray dashed lines correspond to the, respectively, colored points in the shaded relief map.

of the site before being interrupted by a rainstorm; and therefore, a survey on 15 July 2011 covered the same half-site survey area as 12 July. The entire site was resurveyed on 1 May 2012. Herein, a survey is defined as an entire campaign that consists of multiple scan positions. Consequently, a single survey is composed of a point cloud from multiple scan positions that have been coregistered. Because of the steep terrain, we scanned the slopes from the bottom, top, and both sides. Even though we had a scanner that was accurate up to 400 m, the scanner was usually less than 100 m from the ground that was being scanned.

For each terrestrial lidar survey, we used a tripod-mounted Riegl VZ-400 lidar scanner. This system functions by sending a light pulse from the scanner to a surface being scanned and then measuring the time until the light pulse returns to the scanner (if the light pulse hits multiple objects, it will result in multiple returns). The traveltime is converted to the distance from the scanner, and all the points obtained from this process are amalgamated to create a 3-D point cloud. The scanner operates in a near-infrared wavelength (800–1000 nm), and the maximum scanner range varies from 60 to 600 m, depending on object brightness. The scanner accuracy (i.e., the difference between the true value and measured value) is ± 5 mm, and the precision, or repeatability, is ± 3 mm [*Riegl*, 2012].

During each terrestrial lidar survey we set up the tripod and scanner at 9–14 separate scan positions. We used many scan positions because at any location on the study site, the ground surface was partially obscured by standing tree trunks. To establish reference points, we placed over 100 reflective targets on tree trunks (near the base for stability) in a uniformly distributed, random placement from the top to the bottom of the hillslope. Four georeferenced benchmarks were established on rock outcrops at the corners of the site. The real-world coordinates of these benchmarks were obtained using a differentially corrected TopCon GPS, in order to place

Table 1. Erosional Volume, Net Elevation Change, and Erosion Per Unit Area Within Each Morphological Unit Between Lidar Surveys

	Morphologic Unit[a]	Upper Hillslope	Planar Slope	Lower Hillslope	Boulder Field	Divergent	Convergent	
	Mean slope (deg)	20	28	24	28	26	26	
	Area half site (m^2)	N/A	685.20	474.30	263.40	235.40	219.50	
								Total
7 Oct 2010 to 18 Oct 2010	Volume (m^3)	N/A	−2.79	−1.16	−1.57	−2.17	−0.91	−8.60
	Net elevation change (cm)	N/A	−0.41	−0.18	−0.60	−0.92	−0.43	−2.54
	Erosion/area (ton ha^{-1})	N/A	−35.00	−15.74	−51.27	−79.07	−37.26	−218.35
18 Oct 2010 to 12 Jul 2011	Volume (m^3)	N/A	−3.25	−4.24	−1.75	−0.32	−4.44	−14.00
	Net elevation change (cm)	N/A	−0.48	−0.89	−0.67	−0.14	−2.12	−4.29
	Erosion/area (ton ha^{-1})	N/A	−71.78	−135.01	−101.14	−20.46	−319.59	−647.97
12 Jul 2011 to 15 Jul 2011	Volume (m^3)	N/A	−1.06	−2.01	−0.74	−0.27	−0.82	−4.90
	Net elevation change (cm)	N/A	−0.15	−0.42	−0.28	−0.11	−0.39	−1.37
	Erosion/area (ton ha^{-1})	N/A	−23.36	−64.17	−42.75	−17.33	−58.79	−206.40
15 Jul 2011 to 1 May 2012	Volume (m^3)	N/A	0.74	−1.81	−2.33	4.21×10^{-2}	−0.27	−3.63
	Net elevation change (cm)	N/A	0.11	−0.38	−0.89	1.79×10^{-2}	−0.13	−1.26
	Erosion/area (ton ha^{-1})	N/A	9.83	−32.94	−76.20	1.54	−10.94	−108.71
	Area full site (m^2)	2903.75	831.37	635.70	339.53	235.37	708.62	
7 Oct 2010 to 1 May 2012	Volume (m^3)	−30.22	−8.19	−0.76	−5.40	−1.39	−13.61	−59.57
	Net elevation change (cm)	−1.04	−0.99	−0.12	−1.60	−0.59	−1.92	−6.26
	Erosion/area (ton ha^{-1})	−131.53	−124.28	−15.12	−201.36	−74.15	−242.01	−788.46

[a]See Figure 7 for a map of morphologic units.

the point clouds into a global coordinate system. All point clouds were transformed by the same four points (obtained during the first survey); thus, there was no GPS error introduced as one might expect if new GPS measurements were obtained for each survey. Point clouds from individual scan positions were assembled into a single large point cloud using the targets. The number of targets used for alignment ranged from 15 to 35 for any two point clouds, and no point cloud alignment was accepted that had a root-mean-square (RMS) error larger than 0.005 m (although the majority of alignments had lower RMS errors).

3.2. Lidar Data Processing

At the field location, dead, burned trees were still standing during the surveys, and these needed to be removed from the point cloud in order to construct a digital elevation model (DEM). We used the software Terrascan (version 011.018) [*Terrasolid Software*, 2011] to classify and thin points within each point cloud in a consistent manner. Points were classified into three categories: bare ground, low debris (such as loose rocks and fallen logs), or high vegetation (standing trees). To identify trees, a user specifies the steepest allowable slope of the ground terrain. Points steeper than the threshold slope were automatically reclassified as "high vegetation" and "low debris," depending on the height. In the early scans we used points that were classified as both bare ground and low debris in DEM generation; and therefore, the DEMs include fallen logs and small boulders (Figure 3). However, on 1 May 2012 survey there was a nonnegligible amount of herbaceous ground vegetation that had emerged earlier that spring. Therefore, to avoid incorporating plants in DEM topography, we used only the points classified as bare ground to generate a DEM for that survey. After point classification, we thinned the points by taking the average point elevation value of the bare-ground and low-debris points using a radius of 0.005 m. This reduced the point cloud by approximately 10 times.

3.2.1. Point Cloud Interpolation

After a lidar point cloud was processed to remove vegetation, the final point clouds were clipped to a boundary limited to areas of the highest data density. When possible, the watershed boundary was used as the clipping extent. For the top of the watershed, a visual judgment was made as to where the data became more sparse. We converted the data to a triangulated irregular network (TIN) and subsequently interpolated the TIN to a DEM in ArcGIS 10.1 with the TIN to Raster tool using the linear interpolation method. We chose the

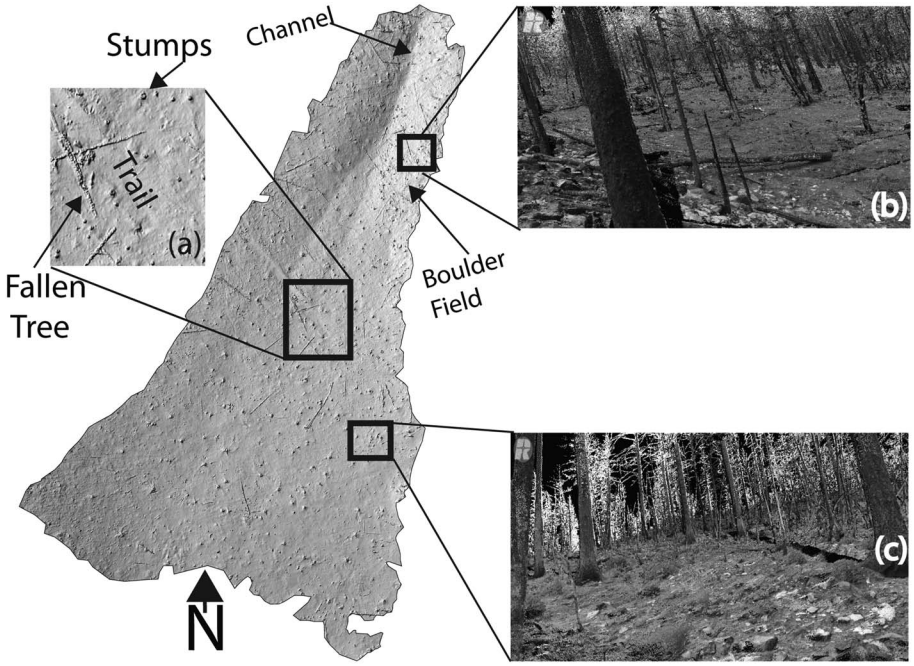

Figure 3. Bare ground DEM showing microtopography such as a boulder field on the east side of the watershed. Downslope is to the north-north east. (a) Close-up view shows standing trees are filtered out, but some fallen trees, boulders, and tree stumps are left in the DEM. (b) Southwest view upslope of lidar points with the boulder field on the left side (1 May 2012). (c) Southern view upslope of lidar points (1 May 2012). Lidar points show exposed cobbles and boulders on the upper hillslope surrounded by erodible soil.

DEM pixel size based on an analysis comparing the number of raw data points per pixel with the pixel size (Figure 4). An inappropriate DEM pixel size can cause interpolation errors [*Lane et al.*, 2003], but there is no universal method for choosing pixel dimensions [*Hengl*, 2006]. The choice of pixel size was based on two competing considerations: (1) pixels interpolated from many points give less weight to erroneous points, but (2) large pixels can misrepresent landscape features [*Brasington et al.*, 2000]. We found that a 15 cm pixel size provided a reasonable compromise, with only 2.5% of the pixels having 1 point per pixel (as compared to 22% for a 5 cm grid).

3.2.2. Ground Surface Occlusion and Low-Point Density Regions

Ground surface occlusion occurs at the study site due to shadows from natural features such as boulders and trees, and this results in gaps in the point cloud. To remove occluded areas, any DEM pixels with a point density lower than 100 point/m^2 were removed from the unvegetated unthinned point cloud. In addition,

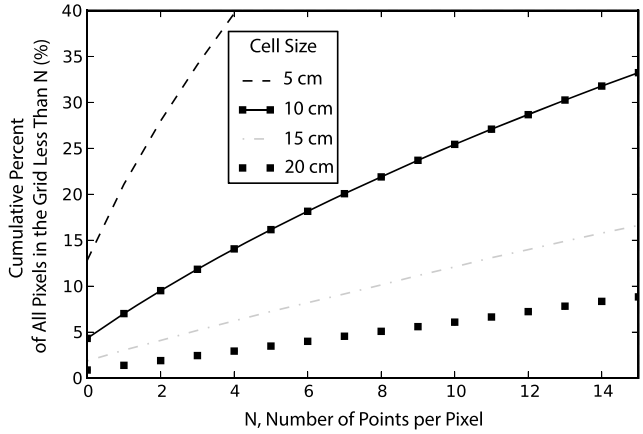

Figure 4. Number of points per pixel versus the cumulative percent of pixels within an entire raster grid as a function of pixel size.

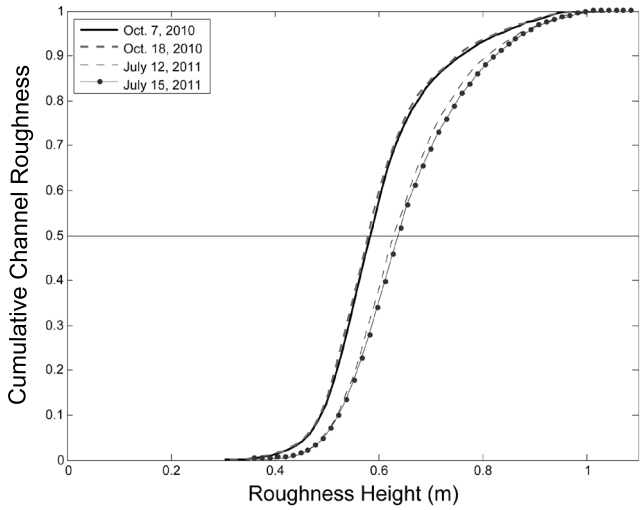

Figure 5. Cumulative fraction of roughness height in the channel. Note the 5 cm difference in median roughness height between the October 2010 and July 2011 scans.

we endeavored to minimize the effect of occlusion through multiple scan positions and an appropriate pixel size for the data density.

Shadowing from trees at the top of the study area creates low-point density regions resulting in a radial pattern of alternating high and low point density. The effect is not present at the bottom of the site because the scan area is narrower, making it possible to exclude areas affected by shadows. Within the low-point density shadow areas, two patterns emerge. Sometimes the erosion/deposition pattern is similar to the surrounding high-point density areas (Figure S3 in the supporting information). In other cases, elevation data are skewed to be higher (Figure S3). This occurs because oblique scan positions are the only source of elevation in the shadow areas, which can result in the preferential sampling of objects above the ground. Biased elevation estimates in the shadow areas are removed using the point density threshold and uncertainty methods. This results in a radial pattern at the top of the site, which is the result of excluding areas of low point density and it is not related to misalignment (see supporting information).

3.3. Uncertainty Analysis

DEMs derived from the point clouds were differenced to show sediment redistribution patterns. The resulting grid is referred to as a DEM of difference (DoD). The minimum level of detection (LoD), which is the smallest measurable elevation change between two surveys, is set by the uncertainty in topographic measurements [*Brasington et al.*, 2000; *Wheaton*, 2008]. The LoD determines whether an elevation difference between two DEM pixels is considered to be real erosion or measurement uncertainty. The LoD therefore is the minimum limit whereby it is possible to quantify erosional estimates.

We quantified lidar survey uncertainty using a spatially distributed approach. To determine the maximum uncertainty between two lidar surveys, *Collins et al.* [2012] proposed the idea of empirical error, which is the uncertainty of two point clouds from some immovable object such as a large rock outcrop (i.e., maximum point offset in any x, y, or z direction). At the field site, four large unchanging rock outcrops represented by hundreds of points in a point cloud were used to calculate an empirical error between TLS surveys. The maximum point offset between two surveys in any direction (x, y, and z) on the rock outcrops was 2 cm. Note that this was not a systematic offset or coregistration error between two point clouds of the same survey, but the maximum offset between two different surveys. Consequently, this value was used as the maximum uncertainty between surveys. However, many portions of the point cloud fit better than the maximum uncertainty; and therefore, we used the methods outlined by *Wheaton et al.* [2010] to calculate a spatially distributed uncertainty.

Uncertainty in point measurement and point processing is associated with certain variables in topographic surveys including high slope angles [*Hodgson and Bresnahan*, 2004], high local terrain roughness (LTR) [*Milan et al.*, 2011], wet areas in fluvial environments [*Lane et al.*, 2003], point density, range, incidence angle, and 3-D GPS point quality [*Wheaton*, 2008]. *Wheaton* [2008] developed an efficient method for estimating the

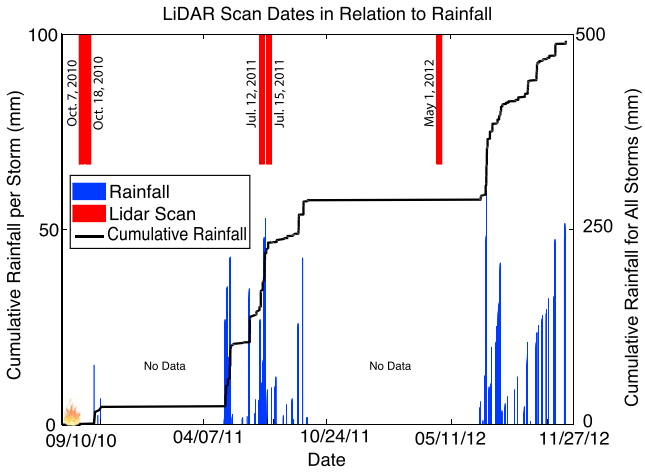

Figure 6. Rainfall measured from a recording, tipping-bucket rain gage. The dates of lidar scans are plotted on the top axis showing the rain storms that occurred between lidar surveys. Cumulative rainfall per storm is shown in blue, and the cumulative rainfall for the entire study period is shown in black.

uncertainty contributed by several of these variables to each pixel within a DEM using a fuzzy inference system (FIS). We developed a FIS based on slope, point density, and local terrain roughness (LTR). Here we define LTR as the difference between maximum and minimum height within a circular window of radius 0.5 m (this results in a similar roughness estimate compared to a slope-normalized approach, see Figure S8 in the supporting information). For each pixel in a DEM, the FIS assigns an uncertainty value, σ_{pix} (m). Values of σ_{pix} ranged between 0.005 m (scanner accuracy) and 0.02 m (the empirical error), with the highest uncertainty in pixels with a steep slope (>27°), high LTR (> 0.5 m), and low point density (<1066 points per m^2). The lowest uncertainty value was assigned to pixels with a gentle slope (< 20°), low LTR (<0.37 m), and a high point density (>13,000 points per m^2). These values were based on the quartiles for each of the variables, such that high values were larger than 75% of the variable range, and the low values were less than 25% of the variable value range. The total elevation uncertainty in each pixel of a DoD is determined as [*Lane et al.*, 2003; *Wheaton*, 2008]

$$\delta = \sqrt{(\sigma_{pix2})^2 + (\sigma_{pix1})^2} \tag{1}$$

where δ is the combined uncertainty based on two surveys, and σ_{pix} is the estimated uncertainty at a single pixel in the DEM corresponding to successive surveys, time 1 and 2, respectively. This combined uncertainty was used to determine the probability of actual change using the *t* statistic [*Wheaton*, 2008]

$$t = \frac{|Z_{pix2} - Z_{pix1}|}{\delta} \tag{2}$$

where Z_{pix} is the pixel elevation of DEMs from successive surveys, time 1 and 2, respectively. Using the *t* statistic, a 95% confidence interval for the LoD can be obtained. Any elevation change less than the LoD is ignored. We applied equations (1) and (2) to the DEMs using the Geomorphic Change Detection (GCD) tool version 5.2.0.0 [*Wheaton*, 2014].

The probability of true erosion/deposition within each pixel is subsequently updated based on the state (erosional/depositional) of surrounding pixels. *Wheaton et al.* [2010] noted that there is a spatial coherence within a landscape such that erosion and deposition tend to occur in contiguous patches, and they present a method to update erosional/depositional probability of a pixel using a spatial coherence filter and Bayes' theorem. Here we use their method within the GCD software by using a 5 × 5 pixel window to create a spatial coherence filter labeling patches of pixels as either erosional, depositional, or below the LoD. If a pixel is within a primarily erosional window and shows erosion, it may be labeled as "below LoD" based on the FIS uncertainty methods that have been applied. However, a new probability for the pixel is determined using the a priori probability calculated with the FIS uncertainty and the a posteriori probability determined with the spatial coherence filter. *Wheaton et al.* [2010] show how these two probabilities can be incorporated into Bayes' theorem, and using a linear transform function the probability of real erosion or deposition for a pixel is updated. Thus, the spatial coherence filter allows adjacent information to inform determinations of whether erosion/deposition is real.

Table 2. Peak Rainfall Characteristics and Peak Runoff Discharge During the Study Period

	Rainfall Characteristics				Peak Discharge			
Date	Average Duration (min)	Average Rainfall Intensity ($mm\ h^{-1}$)	Average Peak 5 min Rainfall Intensity ($mm\ h^{-1}$)	Average Peak 10 min Rainfall Intensity ($mm\ h^{-1}$)	Boulder Field Flume 1-1 (0.069 ha)	Lower Hillslope Flume 1-2 (0.207 ha)	Upper Hillslope Flume 1-3 (0.116 ha)	Convergent Flume 3-1 (0.844 ha)
					(Ls^{-1})			
12 Oct 2010	183	2.7	5.5	6.1	–	–	–	1.2
22 Oct 2010	67.7	5.8	10.7	10.6	–	–	–	1.4
19 Jun 2011	90.4	5.9	22.3	15.2	2.4	> 3.6	0.87	42
30 Jun 2011	10.7	19.8	33.9	16.7	0.0071	0.012	0.085	0.0015
5 Jul 2011	15.7	16.1	33.9	19.8	no runoff			
7 Jul 2011	22.5	46.3	79.8	72.0	> 3.3	> 3.3	> 3.6	> 45
10 Jul 2011	31.8	13.8	37.3	25.9	3.5	3.6	3.6	46
12 Jul 2011	37.5	6.5	18.1	11.8	0.042	0.032	0.236	–
13 Jul 2011	13.7	46.6	76.9	51.0	sediment filled flume			
14 Jul 2011	25.2	11.1	29.1	13.5	sediment filled flume			
14 Jul 2011	23.0	17.9	29.3	18.3	sediment filled flume			
16 Jul 2011	26.6	7.9	30.0		0.0081	0.063	0.033	0.076
19 Jul 2011	47.0	8.3	27.5	22.0	3.5	3.6	3.2	–
19 Aug 2011	12.4	6.7	7.7	8.8	no runoff			
7 Sep 2011	376.2	2.4	10.5	12.0	3.1	3.5	4	29

3.4. Net Erosion and Deposition

After incorporating uncertainty into a DoD, it is possible to estimate the net erosion and deposition between surveys. The erosional or depositional depth of a pixel is multiplied by the pixel area to determine a volume of change (Table 1). This volume is multiplied by the soil bulk density (Table S1) to estimate the total mass of sediment removed. We used a bulk density of 0.86 g/cm^3 to determine the mass of erosion between the first two surveys, when ash composed part of the eroded material. For the rest of the surveys we used a bulk density of 1.51 g/cm^3, which is the average from many samples collected in 2011 (Table S1). Finally, we estimated erosion per unit area rather than sediment yield. Sediment yield is usually expressed in terms of mass per area per year. Because the timing of erosion is related to the duration of water flow, normalizing the mass per area per year may lead to misconceptions about the continuity of erosion or deposition processes. Consequently, we use the definition of erosion per unit area (ton ha^{-1}), which is a metric used in other studies [e.g., *Shakesby and Doerr*, 2006].

3.5. Local Terrain Roughness

We examined the roughness evolution for the first four surveys within the small (half-site) survey area of the 12 and 15 July 2011 surveys (Figure 5). During the digital tree removal using Terrascan, trees were cutoff at 40 cm above the ground for all point clouds. This arbitrarily skews the roughness distribution. However, because the technique was consistent on all point clouds, relative changes in roughness can be observed.

3.6. Site Measurements

Rainfall data were collected for cyclonic and convective rain storms at the study site [*Ebel et al.*, 2012a; *Moody and Ebel*, 2013]. Rainfall was measured with three recording tipping-bucket rain gages (model R2, Onset Corp.) maintained during rainfall months (approximately April to October) (locations shown in Figure 2). These rain gages were used to determine the cumulative rainfall between lidar surveys (Figure 6) and rainfall intensities (Table 2). The rain gages recorded similar values during each precipitation event, suggesting that observed spatial variation of erosion/deposition was not due to spatial variation of precipitation.

Water discharge (Ls^{-1}) was measured in microdrainages on the hillslope and at the outlet of the first-order channel (Figure 2a). Three, 2.54 cm modified Parshall flumes were deployed on the hillslopes and one 7.62 cm modified Parshall flume was deployed in the channel (Figure 2a and Table 2) [*Ebel et al.*, 2012a].

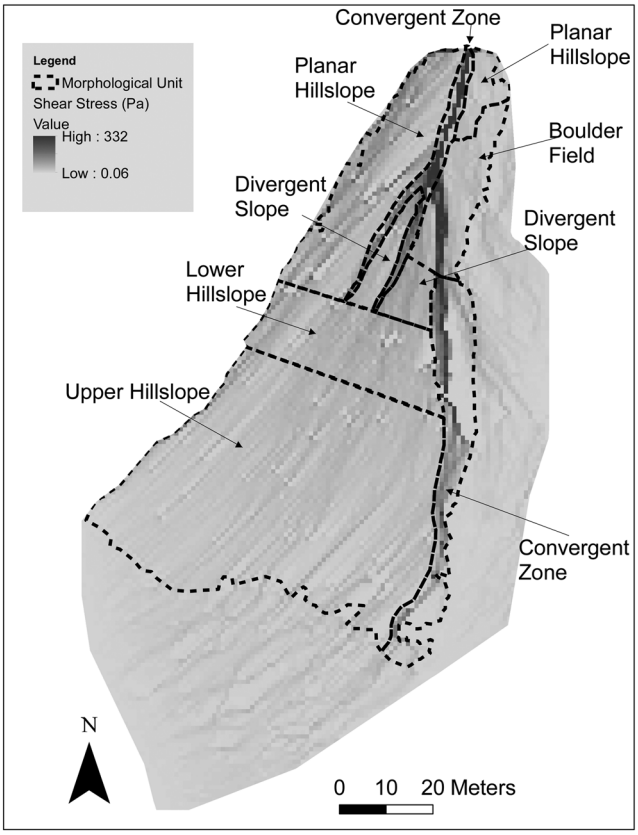

Figure 7. Spatial distribution of maximum shear stress predicted by equation (6) using the peak runoff rate from 10 July 2011. Linear patterns indicate the flow lines. Morphologic units within the area of TLS data acquisition are labeled. The southern unlabeled region is a ridge, and the eastern unlabeled region is occupied by a rock outcrop. These areas fall outside of the TLS data; the elevation values are derived from airborne lidar.

Ultrasonic sensors (M5000, Massa Products Corp, Hingham, Massachusetts. *Ebel et al.*, 2012a] were mounted over the throat of each flume to measure water depth every 10 s. Sediment was sometimes deposited in the flume during the falling limb of the hydrograph, but often the peak discharge was recorded (Table 2).

3.7. Estimating Overland Flow Shear Stress

Erosion by overland flow depends on the excess boundary shear stress [*Howard and Kerby*, 1983; *Sanford and Maa*, 2001]. To explore the hypothesis that overland flow was the major driver of sediment erosion at the study site, we sought to understand the relationship between erosion and shear stress. We estimated the maximum shear stress for every pixel in the study area using the largest measured runoff rate during the monitoring period (10 July 2011, 46 Ls^{-1}). Using a simplified approach, we assumed that Hortonian runoff was uniform across the site. The predicted maximum shear stress (τ_{max}) was determined using a similar approach to that of *Dietrich et al.* [1993]:

$$\tau_{max} = \rho g h S \tag{3}$$

where ρ (kg m^{-3}) is water density, g (m s^{-2}) is gravitational acceleration, h (m) is the water depth, S is $\sin\alpha$, and α is the local slope angle. If we consider the standard formulation for Manning's equation and substitute water depth for the hydraulic radius, we obtain

$$V = \frac{h^{\frac{2}{3}} S^{\frac{1}{2}}}{n} \tag{4}$$

where n is Manning's roughness coefficient and V (m s^{-1}) is depth-averaged velocity. We measured n on the hillslopes at four locations by measuring velocity (via the traveltime of acrylic paint balls between two known distances), flow depth (ruler), and ground slope (level), and solving for Manning's n. The average value was n

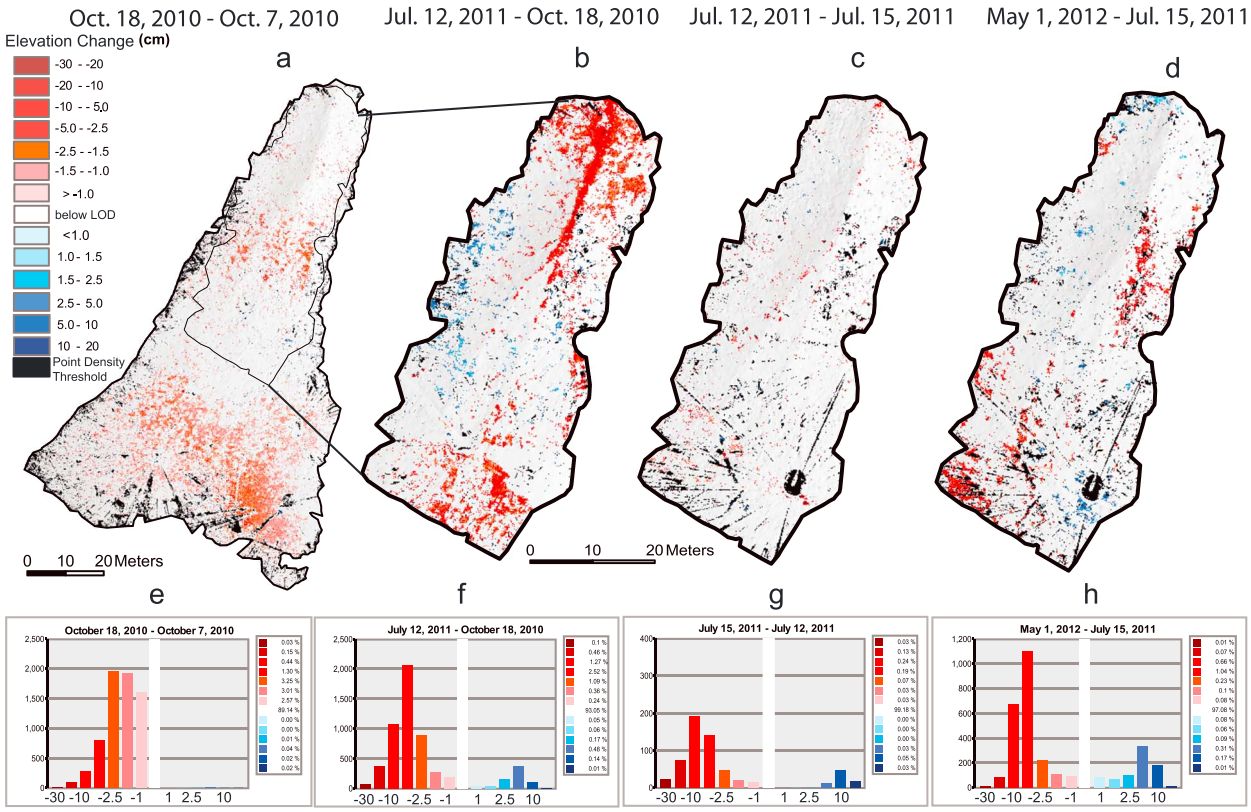

Figure 8. Geomorphic change detection grids showing patterns of erosion. (a–d) DEMs of Difference (DoDs) between each of the lidar surveys showing erosion and deposition patterns. (e–h) Histograms showing the distribution of erosion and deposition. The colors in the histograms correspond to the colors and erosion/deposition values in the legend.

$= 0.21 \pm 0.07\ \mathrm{m}^{-1/3}\ s$, which was used for the entire DEM. We converted the flow velocity to unit discharge by multiplying both sides of equation (4) by the water depth, h. Rearranging to solve for h, we obtain

$$h = \frac{q^{\frac{3}{5}} n^{\frac{3}{5}}}{S^{\frac{3}{10}}} \tag{5}$$

where q is the discharge per unit width. Substituting equation (5) into equation (3), we find:

$$\tau = \rho g q^{\frac{3}{5}} n^{\frac{3}{5}} S^{\frac{7}{10}} \tag{6}$$

Equation (6) was applied on a pixel by pixel basis, with q_i for the ith pixel defined as

$$q_i = \frac{A_i Q_{\max}}{b_i A_{\mathrm{flume}}} \tag{7}$$

where A_i (m^2) is the drainage area contributing to the pixel, $Q_{\max}$ (Ls^{-1}) is the maximum discharge measured at the outlet of the drainage basin, b_i is the pixel width, and A_{flume} is the drainage area of the flume at the outlet of the basin (Figure 2b).

The drainage area was determined from a DEM of the site using the D-infinity method in the tauDEM software (version 5.1.1) [*Tarboton*, 1997]. Within the study drainage basin, a small area of topography near the basin margins was not captured by terrestrial lidar surveys. Consequently, we used airborne lidar data from August 2010 to fill in data gaps of the unsurveyed areas. The airborne lidar was combined with the terrestrial lidar data from the 1 May 2012 survey, which most accurately captures the final drainage pattern. These data were joined to create a DEM with a 0.9 m pixel grid, which best represents the airborne lidar point density and also prevents small-scale boulder or tree features from dominating the shear stress calculation by creating very steep slopes (Figure 7).

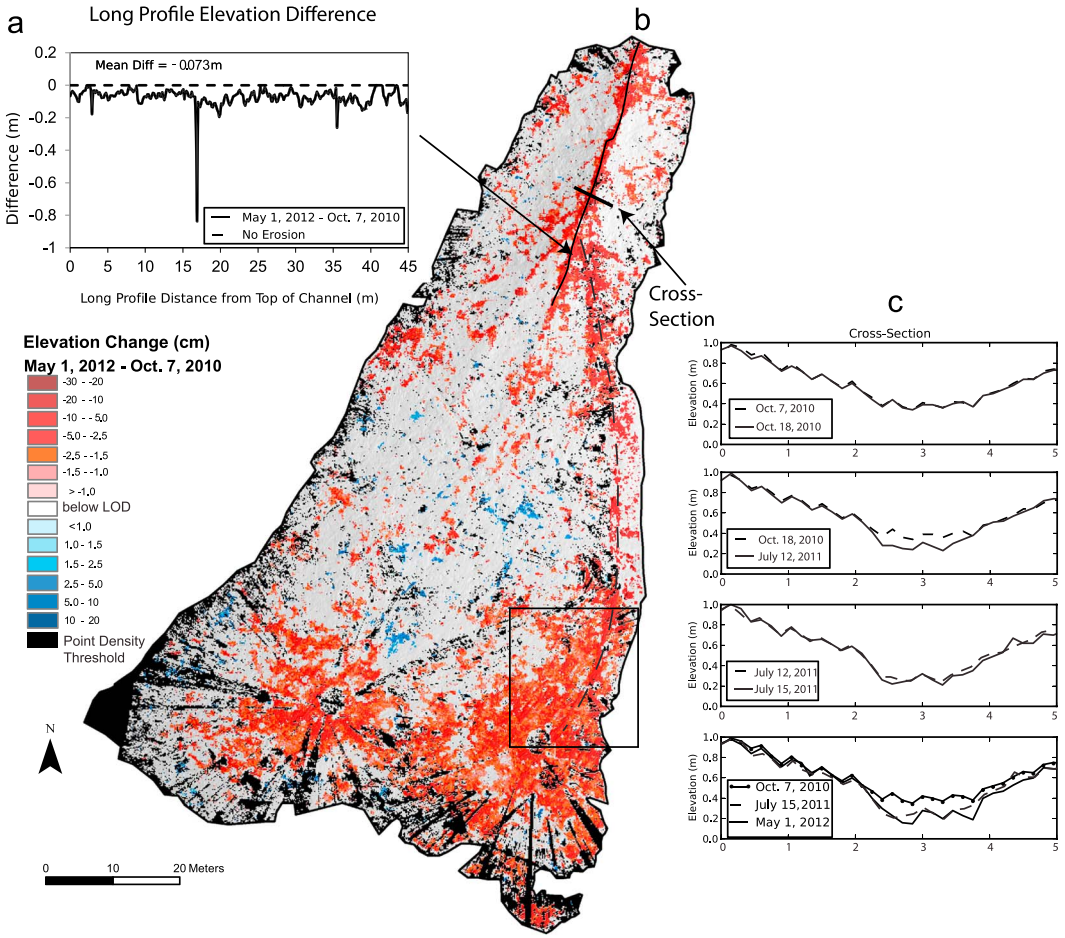

Figure 9. (a) Channel change along the longitudinal profile, with a mean of 10.4 cm. (b) DoD between the first and last lidar surveys. The dashed line shows a subtle channelized feature, showing a path of sediment transport from the top to the bottom of the site. The thin black solid line represents the location of the longitudinal profile in Figure 9a, and the thick black solid line represents the location of the cross section in Figure 9c. The solid box denotes the location of Figure 10. Note that the change map is slightly transparent and underlain by the May 2012 hillshade topography. It is also displayed on a 2.5 cm grid for clarity. (c) Cross sections showing channel change over time.

3.8. Morphologic Units

The site was divided qualitatively into a set of distinct morphological units based on slope, curvature, and drainage area (Figure 7). The hillslope was separated into a lower hillslope (average slope angle 24°) and an upper hillslope that is less steep, with an average slope angle of 20°. The convergent unit was identified by sharp changes in planform curvature and a high drainage area. Planar hillslopes were identified as areas with little curvature, and convex-upward areas between channel-like features were classified as divergent slopes. Finally, an area that contained an unusually dense and prominent collection of boulders was classified as a boulder field. Areas outside the TLS survey footprint to the east were occupied by a rocky outcrop, and to the south a ridge with relatively smooth topography (Figure 7). These regions are not included in the analysis of morphologic units because there is sparse TLS data in those areas.

4. Results

4.1. Uncertainty

The incorporation of uncertainty into lidar change detection allowed us to detect true erosion and deposition within a 95% confidence interval. In general, uncertainty increases downslope as the gradient increases and remains low in areas toward the upper slope where roughness is low (Figure S15). These trends are modulated by variations in point density, which also affect uncertainty but do not vary consistently in space. In order to separate true elevation change from measurement uncertainty, any values below the LoD have been

Table 3. Median Local Terrain Roughness by Morphologic Unit

Date	Planar Slope (m)	Lower Hillslope (m)	Boulder Field (m)	Divergent (m)	Convergent (m)	Channel Only (m)	Hillslope Only (m)
7 Oct 2010	0.52	0.48	0.61	0.51	0.49	0.58	0.53
18 Oct 2010	0.52	0.48	0.62	0.5	0.49	0.58	0.52
12 Jul 2011	0.59	0.53	0.62	0.52	0.51	0.63	0.57
15 Jul 2011	0.60	0.52	0.63	0.52	0.51	0.64	0.58

removed from histograms of change in Figure 8 and assigned to the category "below LoD." For this reason, the histograms appear bimodal because the small central values have been removed (Figure 8).

4.2. Net Erosion and Deposition in Morphological Units

Over the entire study period (7 October 2010 to 1 May 2012), the upper hillslope generated the most erosion in volumetric terms. The next largest erosion volume was derived from the convergent unit (Table 1). If the convergent unit is considered as the area of potential channelized erosion and the remaining morphological units function as contributing hillslope, then the total hillslope erosion volume was 3 times larger than erosion in the convergent unit. However, the eroded volume per unit area from the convergent unit was still greater than the hillslope morphological units. The measured net erosion (Table 1) using terrestrial lidar falls within the range of values determined from point measurements of post-wildfire erosion in other settings (0–414 ton ha^{-1}) [*Shakesby and Doerr*, 2006]. Note that the lidar study area does not encompass an entire watershed, so the total volume of sediment erosion measured between surveys can incorporate incoming sediment from sources outside of the lidar survey areas. Moreover, there may have been erosional channels between the patches of erosion (Figure 9), but deposition between surveys can obscure small pathways.

The variability in erosion between morphologic units changes over time. During the first period (7 October 2010 to 18 October 2010) net erosion was similar and had substantially less variability between morphologic units (coefficient of variation, COV = 0.18) than the variability between morphological units for the later three time periods (COV = 0.76, 0.90, and 1.06, respectively).

4.3. Patterns of Erosion and Deposition

The lidar surveys bracketed several significant rain storms, between which we observed an evolving pattern of erosion and deposition. The first rainstorm on 12 October 2010 had a 5 min rainfall intensity (I_5) of 5.5 mm h^{-1}. The pattern of erosion detected by the DoD after this first rainstorm was discontinuous, relatively minor, and primarily concentrated within the upper hillslope with little deposition (Figure 8a). By contrast, erosion between 18 October 2010 and 12 July 2011 was concentrated primarily in the convergent unit (red pixels in Figure 8b) resulting from substantial runoff during thunderstorms on 19 June 2011 and 7 July 2011 with peak I_5 = 80 mm h^{-1} (Figure 6 and Table 2). The convergent unit eroded 2.6 times the volume of the boulder field after the first summer thunderstorms in 2011 (Table 1).

Several convective storms took place between 12 and 14 July 2011, with peak I_5 = 77 mm/h (Table 2). Unlike the previous thunderstorms that caused concentrated erosion, the DoD between 12 July 2011 and 15 July 2011 shows patchy erosion with discontinuous channel erosion (Figure 8c). Field observations and photos reveal that erosional patches primarily represent lowering between boulders, cobbles, and tree trunks (see supporting information). The pattern of erosion over about a year between 15 July 2011 and 1 May 2012 (Figure 8d) indicates essentially no concentrated erosion but moderate erosion in the boulder field and in the lower hillslope unit. Peak I_5 was 30 mm h^{-1}, and erosion during this time was observed to occur between roughness elements. Note that in the time between the 15 July 2011 and 1 May 2012 surveys, pioneer shrubs and grass had taken root on the site, which also may have limited erosion. The last DoD showed more than 8 times the erosional volume from the boulder field compared to the convergent unit (Table 1 and Figure 8). This was mostly due to a decrease in erosion from the convergent unit rather than an increase in erosion from the boulder field.

The pattern of net erosion and deposition during the entire study period is illustrated in a DoD between the first and last lidar surveys (7 October 2010 and 1 May 2012) (Figure 9b). Major areas of erosion are concentrated on the upper hillslope, the convergent slopes, and the boulder field. The average erosion depth was 7.3 cm along the longitudinal profile of the main channel (Figure 9a). Little deposition is seen in the longitudinal profile, indicating that sediment is transported out of the watershed, and not stored in the channels. A time

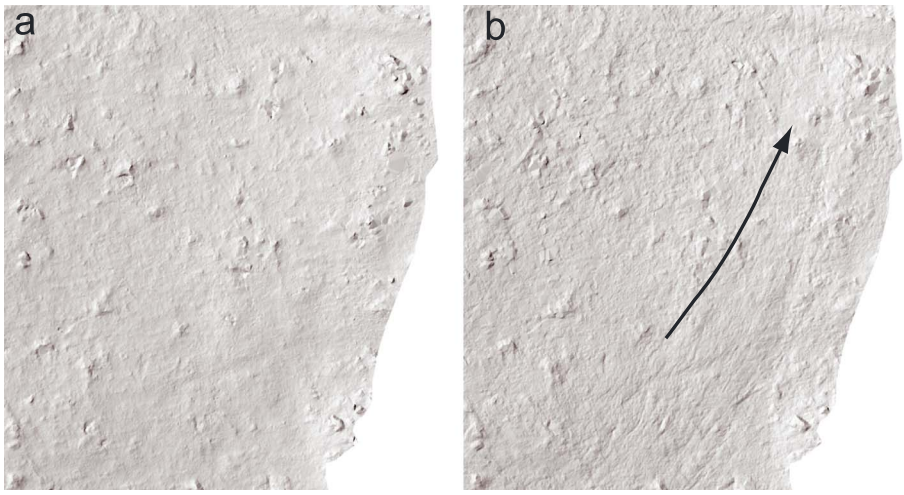

Figure 10. Shaded relief map showing relatively smooth terrain on the upper hillslope on (a) 7 October 2010 compared to (b) 1 May 2012 where the terrain is dissected by discontinuous rills and rivulets. Arrow shows direction of flow.

sequence of channel change along a cross section (Figure 9c) shows that most erosion occurred in the first summer after the wildfire, and that the channel underwent smaller adjustments during subsequent storms. Sediment eroded from the watershed accumulated in the downstream flume or passed through the flume downstream.

4.4. Local Terrain Roughness

The median LTR shows an increase in roughness between 18 October 2010 and 12 July 2011 in most morphologic units (Table 3). To understand the change in roughness we divided the half-site study area into two categories: hillslope and channel. The channel in this analysis is a subunit of the convergent unit, with clearly defined channel banks. The channel was defined by a sharp change in slope curvature, and the hillslope represented the survey area outside of the channel.

We found that the median roughness in both the channel (Figure 5) and the hillslope (Table 3) areas showed a distinct increase between 18 October 2010 and 12 July 2011. This period included four relatively intense rain storms on 19 and 30 June 2011 and on 7 and 10 July 2011 (Table 2). Little change was detected between 12 and 15 July 2011, despite the fact that this short interval included one of the most intense rain storms (I_5 = 77 mm h^{-1}, 13 July 2011). The median site roughness values in the channel and on the hillslopes both increased by approximately 5 cm after the 19 June and 7 July 2011 storms, but little change occurred between 12 and 15 July 2011.

4.5. Shear Stress

A simple relation between erosion depth and shear stress was not evident (Figure S14). To unravel the nature of this relationship, we divided the data into four categories. First, we used the mean ash depth of 1.8 cm to separate possible ash erosion from soil erosion. This data cutoff is similar to the median value of all erosion data (2 cm). Second, we separated the shear stress into high and low values based on a flume study of fire-affected soils by *Moody and Nyman* [2013]. Using soil cores from the study site, *Moody and Nyman* [2013] show that the median detachment rate of soil from the site corresponds to a shear stress of 17 Pa. While this criterion does not represent a system threshold, it corresponds with the median shear stress (15 Pa) calculated for the site (Figure 7). The four categories are thus low shear stress/low erosion depth, low shear stress/high erosion depth, high shear stress/low erosion depth, and high shear stress/high erosion depth.

The majority of the landscape (57%) is composed of areas of low shear stress and low erosion depth (Figure S14). These areas appear to be well connected (Figure 11) within the upper hillslope unit. The areas of high shear stress and high erosion depth delineate the zones of concentrated flow and are located primarily in the convergent unit and boulder field. Areas of high shear stress and low erosion depth are observed throughout the lower portions of the site. These areas either correspond to locations of redeposition (i.e., there was high shear stress and high erosion, but redeposition makes it appear that there was little net erosion) or locations

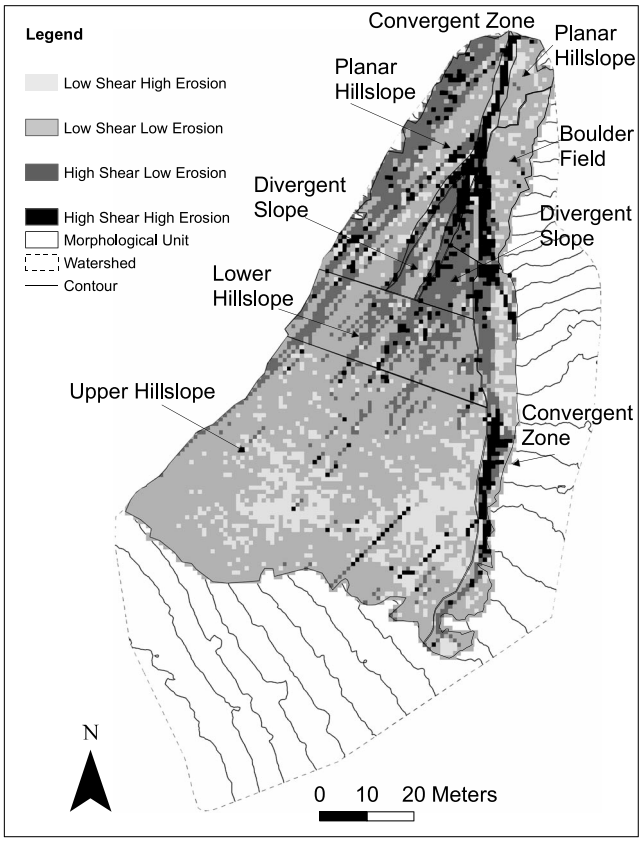

Figure 11. Spatial distribution of shear stress-erosion categories, where shear stress is predicted and erosion is observed.

where cobbles, boulders, bedrock, tree trunks, or tree roots prevent erosion. A few areas of low shear stress and high erosion depth exist throughout the site with a concentrated area on the upper hillslope.

5. Discussion

5.1. Hydrology

During the study there were a variety of precipitation events including long-duration low-intensity frontal storms, short-duration high-intensity convective storms, and snowfall. High runoff was observed after rain storms, even those with moderate intensity (for example, 30 June 2011 and 19 July 2011 (Table 2)), which is consistent with prior studies showing high runoff after wildfire [e.g., *Rubio et al.*, 1997; *Benavides-Solorio and MacDonald*, 2001; *Moody and Martin*, 2001b].

5.2. Sediment Provenance and Erosion Rates

At the field site, we found that the majority of eroded sediment (volumetrically) was derived from relatively shallow erosion on hillslopes rather than from convergent areas (Table 1). Hillslopes contributed 3 times more sediment (by volume) than convergent areas between the first and last survey (Table 1). However, when normalized by surface area the convergent areas contribute a larger depth of sediment (Table 1).

The rate of erosion, however, is not constant with respect to rainfall intensity. Rather, erosion rates evolve as the sediment erodibility changes with time. We contextualized the sediment erosion between lidar surveys in terms of the hydrologic forcing using I_5 (Table 2). Initial erosion in October 2010 was quasi-uniform in space (16–79 ton ha^{-1}, Table 1) and relatively high (3–14 ton ha^{-1}/mm h^{-1}) when the net erosion for each morphological unit is normalized by I_5 = 5.5 mm h^{-1} (Table 2). This is because the sediment composition was mostly ash, as indicated by the bulk sediment densities (0.86–1.36 g cm^{-3}, Table S1). Removal of the ash layer exposed an uncohesive soil layer affected by the wildfire (bulk density 1.31–1.62 g cm^{-3}, Table S1) with a high erodibility [see *Moody and Nyman*, 2013, Table 5]. Later erosion by moderate intensity rainfall (average I_5 = 41.4 mm h^{-1} for 19 June–10 July 2011, Table 2) had normalized erosion rates for the morphological units that ranged from 0.49 to 7.7 ton ha^{-1}/mm h^{-1} (18 October 2010 to 12 July 2011). The soil erodibility again

Figure 12. Photos from the bottom of the field site before and after the 7 July 2011 rainfall event. (a) Photo from 5 November 2010. White arrows indicate boulders that are similar in both photos. (b) Photo from 8 July 2011. Dark grey ash present in November 2010 has been eroded by 8 July 2011 leaving larger cobbles in place. Objects such as embedded boulders and tree roots in the channel are resistive to erosion. (Photo Credit: Brian Ebel).

changed as the easily eroded soil was exhausted and deeper less erodible soil was exposed [see *Moody and Nyman*, 2013, Table 5], resulting in normalized erosion rates of 0.38–1.4 ton ha^{-1}/mm h^{-1} for soil with bulk densities (1.48–1.59 g cm^{-3}) from 12 to 15 July 2011. Normalized erosion rates for the final scan DoD were also low (0.69–4.1 ton ha^{-1}/mm h^{-1}).

5.3. Effects of Roughness

The changing erosion volume corresponds with a change in the erosion distribution in the morphologic units on the landscape (Figure 8 and Table 1). This appears to be in part due to changes in surface roughness (Figure 5) because the highest erosion depths outside of channels correspond to low-roughness areas where more sediment is available (Figure S13).

Both the channels and the surrounding hillslope increased their median roughness by approximately the same amount (5 cm) after the thunderstorms between 19 June and 12 July 2011 (Table 2). If large clasts were moving from the hillslope to the channel, the channel should coarsen and the hillslope should appear less rough. However, the fact that the hillslopes and channel showed similar increases in roughness suggests that fine material was exported simultaneously from the channels and hillslopes, which exposed large particles from the subsurface, resulting in armoring (Figure 12). Another study of post-fire erosion in the Front Range showed similar observations of surface armoring and preferential transport of fine sediment [*Wohl*, 2013].

5.4. Erosion and Shear Stress in Morphological Units

There is a clear visual association between flow convergence, high shear stress, and deep erosion (Figure 9 and 11), despite the fact that a pixel by pixel comparison does not show a strong correlation (Figure S14). We interpret these results as indicating that there is indeed a relationship between overland flow shear stress and erosion, but that the correlation is obscured by one or more additional contributing factors that we consider subsequently.

A comparison of the calculated shear stress in relation to measured erosion (Figure 11) reveals two kinds of anomaly: areas with high shear stress but low erosion depth, and areas that show substantial erosion depth despite low shear stress. We interpret the first type of anomaly as primarily reflecting the presence of essentially immobile materials such as large boulders, bedrock, and tree trunks. All three are common at the study site and are found on hillslopes within the convergent units (Figure 12). In theory, areas with high erosion and redeposition would also fit this anomaly; however, at the field site, field observations make it clear that there is little overall deposition.

There are several potential explanations for the second anomaly (areas that show high erosion depth despite having low shear stress). The variations in erosion depth may reflect variations in sediment erodibility (see discussion in section 5.1), locally high shear erosion not captured by the shear stress estimate, or erosion that was caused by processes other than overland flow erosion. Regarding the last explanation, we consider the possibility of erosion due to five common post-wildfire hillslope erosion processes: landsliding, dry ravel, biogenic creep, frost heave, and rain splash/rainflow. All but one of these can be ruled out as substantial contributors

Table 4. Proportion of Shear Stress-Erosion Categories by Morphologic Unit

Morphologic Unit	High Shear Stress/High Erosion Depth %	High Shear Stress/Low Erosion Depth %	Low Shear Stress/High Erosion Depth %	Low Shear Stress/Low Erosion Depth %
Upper hillslope	1.31	4.98	22.92	70.79
Planar hillslope	7.94	37.69	10.85	43.52
Lower hillslope	3.32	39.72	2.30	54.66
Boulder field	19.86	15.31	12.44	52.39
Divergent slope	8.25	59.79	3.44	28.52
Convergent slope	24.86	27.14	16.19	31.81

to erosion at the site during the monitoring period. No signs of landslides or other forms of mass movement were observed at the site. It is possible to rule out the influence of dry ravel because this typically requires slopes greater than 33°, a typical angle of internal friction [*Gabet*, 2003b]. The areas occupied by slopes greater than 30° on the entire study site represent less than 7% of the total area. In addition, negligible erosion was visually observed by biogenic or freeze-thaw processes over the 2 year observation period. Therefore, the fifth process, rain splash and rainflow likely dominated erosion in regions with low drainage area and shallow overland flow. Rain splash is an important erosion mechanism for detaching sediment particles [*Proffitt et al.*, 1991; *Gabet and Dunne*, 2003]. It is enhanced when detached particles are transported by shallow overland flow depth (a process known as rainflow) [*Moss et al.*, 1979; *Moss*, 1988; *Proffitt et al.*, 1991; *Gabet and Dunne*, 2003]. This is strongly supported by observations of discontinuous rilling on previously unchannelized slopes (Figure 10).

Within individual morphologic units, the shear stress and erosion patterns provide further insight into erosional processes. For example, on the upper hillslope, most of the erosion (71%) was in the low shear stress/low erosion depth category (Table 4). Low erosion is not unexpected on a hillslope without topographic convergence to enhance runoff erosion. However, it is interesting that 56% of the upper hillslope with high erosion (> 1.8 cm) occurred within low LTR areas (Figure S13), suggesting that erosion was strongly enhanced in areas without large obstacles. The low drainage area and lack of channelized erosion suggest that rainflow erosion was the likely erosional mechanism in these areas. Additionally, soil cores collected from this morphologic unit demonstrate relatively high erodibility (see *Moody and Nyman* [2013], data for Fourmile Canyon-North Burned, clusters A, B, and C, in their Table 5). A few linear, high shear stress/high erosion paths (~1–5 m in length) on the upper hillslope appear to be rill erosion (Figures 10 and 11), which were likely eroded by overland flow.

The lower hillslope had a much larger proportion of areas considered high shear stress/low erosion (40%) compared to the upper hillslope unit (5%). The higher shear stress is the result of the steeper slope angle in the lower hillslope unit (Table 1). However, the lower hillslope had a high density of large roughness features (Figure S13), which trapped sediment during downslope movement, reducing erosion (Figure 9). This interpretation is supported by field observations of fresh sediment deposits behind fallen logs on the lower hillslope. Consequently, the lower hillslope had the lowest overall erosion (0.12 cm, normalized by area; Table 1) of any morphologic unit.

Linear patterns associated with channelized erosion were clearly observed in the high shear stress/high erosion areas of the convergent unit (Figure 11). The convergent slopes experienced the highest depth of erosion between the first and last survey (1.92 cm, normalized by area; Table 1). Twenty-seven percent of the convergent unit experienced high shear stress but low erosion (Figure 11 and Table 4). These areas appear to be associated with immobile obstructions (such as boulders, bedrock, and tree trunks). Only 16% of the convergent slope area had anomalously high erosion and low shear stress, which may result from channel bank erosion. For example, channel erosion could have caused localized slumping of the channel banks resulting in high erosion without a high shear stress.

In the boulder field, areas of both high shear stress/high erosion depth and high shear stress/low erosion depth are primarily aligned with the convergent unit (Figure 11). This suggests the process of overland flow

erosion. Despite net erosion within the boulder field (1.60 cm, normalized by area; Table 1), there is little change in the roughness over time ($\leq$ 2 cm; Table 3), indicating relative stability.

The divergent morphologic unit experienced minimal erosion both in terms of total volume (1.39 m^3) and relative depth (0.59 cm) (Table 1). Patches of high shear stress/high erosion were limited (8.25%) but indicate overland flow erosion that was likely enhanced by rain splash (Figure 11). A similar percentage of high shear stress/high erosion pixels was observed on the planar hillslope (7.94%), and this was manifested in linear patterns oriented along flow lines suggesting rilling or channelized erosion (Figure 11).

5.5. Geomorphic Evolution

The erosional response at this study site reveals a geomorphic evolution after the wildfire as mobile sediment is removed by the first rain storms and the site becomes dominated by less mobile material. The initial thunderstorms (19 June to 12 July 2011) produced deep channel erosion (Figure 9c). Later storms of a similar magnitude (13–14 July 2011) generated relatively little erosion and minor deposition in some morphologic units (Figures 8 and 9 and Table 1). This suggests that the threshold for erosion changed after the first thunderstorms. We interpret this change in threshold over time as reflecting changes in controlling factors such as the removal of fine sediment, exposure of effectively immobile boulders, and consequent armoring (Figure 12). It is not possible to discount the fact that early 2011 storms varied from the 13 and 14 July rain storms, which also influence erosional thresholds, but qualitative evidence from site photographs (Figure 12) and quantitative evidence from lidar data show a relative change in surface roughness (Figure 5 and Table 3).

Moreover, there are similarities in the overall geomorphic evolution experienced at this study site and a burned field site described by *Schmidt et al.* [2011] and *Staley et al.* [2014] in the San Gabriel Mountains. For example, most of the material eroded during the first post-wildfire rainstorm at the San Gabriel study site came from the loose material that was excavated from the previously unchannelized valley bottom of the watershed [*Schmidt et al.*, 2011]. During a subsequent storm, most of the erosion was generated from hillslopes [*Staley et al.*, 2014]. While their study site is nearly twice as large, the upper portion of their site showed patches of erosion and deposition similar to the field site in this study [*Staley et al.*, 2014]. One of the chief differences in the post-wildfire response at the two locations was that the San Gabriel site experienced extensive rilling and debris flows, unlike the field site in this study. This is likely attributed to the steeper slopes ($\sim$ 40°average slope at the San Gabriel site) and the lack of standing vegetation and large boulders at that site.

Consequently, the geomorphic response at this study site appears to depend partly on the site characteristics before the wildfire and, in particular, on the relative proportions of fine sediment, boulders, bedrock, and immobile woody debris across the site surface. Many wildfire sites experience extensive rilling during initial rain storms [*DeBano*, 2000; *Staley et al.*, 2014; *Pelletier and Orem*, 2014]. Observed rilling at this study site was discontinuous and restricted in both depth and spatial extent, even after the first rainstorm (Figure 8). We attribute the limited rill erosion to the coarse surface soil texture (see section 2 and *Ebel et al.* [2012b] and *Moody and Nyman* [2013]) and the ubiquitous immobile obstacles (cobbles, boulders, and tree trunks) that create high surface roughness, a factor known to reduce rilling [*Rieke-Zapp et al.*, 2007]. Moreover, the higher erosion on hillslopes relative to convergent units may be related to the drainage density. The stream density at the study site is 7.8 km^{-1}. This is less than stream densities for other burned landscapes in the region (21–48 km^{-1}) in which channel erosion composed 80% of the total erosion and hillslope erosion only 20% [*Moody and Martin*, 2001a]. Although we cannot rule out that more rilling may have occurred if the site was subjected to more high intensity thunderstorms.

Finally, the observed post-wildfire erosion leaves a geomorphic legacy, which will influence the future site evolution. Scour has deepened the channel so that as vegetation density increases, hillslope creep will probably replace overland flow as the major erosional process, and the channel should refill with sediment. On most of the site, and especially the boulder field, erosion of the fine soil matrix has left boulders and cobbles exposed, leading to an armored hillslope. The loss of soil combined with the high burn severity throughout the study area will require time for new soil development.

6. Conclusions

This study demonstrates that the highest volume of erosion occurred on hillslopes (87% of the study area), which contributed more than 3 times as much sediment loss as convergent areas (13% of the study area). However, the erosion depth (volume/area) was higher in convergent areas (Table 1), which led to channel

deepening relative to the surrounding hillslopes (Figures 9b and 9c). Moreover, the greatest hillslope erosional response occurred in areas with relatively low surface roughness and deeper soils (Figure S13). The correspondence between erosion depth, sediment particle size, and roughness suggests that the post-wildfire erosional response was conditioned in part by the availability of erodible sediment.

Additionally, terrestrial lidar makes it possible to observe the geomorphic evolution of the site. The first summer thunderstorms on the study site generated channel incision and led to hillslope and channel coarsening. Subsequent thunderstorms of a similar magnitude had a limited effect on channel erosion, as available sediment was depleted and channel roughness had increased. This suggests that progressive channel armoring led to a decline in erosion over the 20 month study period. Adjacent hillslopes armored to a similar degree. This indicates that large clasts did not move from the hillslope to the channel but were exposed in situ as fine sediment was eroded from the hillslopes and the channels. During the last two lidar surveys, erosion was limited to the export of fine sediment from between roughness elements such as tree trunks and boulders.

The geomorphic legacy after wildfire erosion at the study site shows an overall hillslope and channel coarsening, channel deepening, and an export of fine material. This state reflects the post-fire hydrology and pre-fire site conditions. The post-fire hydrology encouraged the export of fine sediment from the site, and the large boulders and cobbles that armored the surface (Figure 12) were a function of the pre-fire grain size distribution. The coarse sediment that emerged from the soil matrix and immobile tree trunks were sufficiently large to prevent extensive rill development. Moreover, slope angles at the site were insufficient for mass failure and dry ravel erosion. The future geomorphic processes expected at the site are hillslope soil development, diffusion of soil from hillslopes to fill the incised channels, and sediment anchoring from new vegetation growth.

Acknowledgments
This study was supported by the National Science Foundation (grants EAR-0952247 and EAR-1323137 to G.T.). We are grateful for lidar equipment and support from David Phillips and UNAVCO staff, lidar processing advice and software from Steve DeLong and Joe Wheaton. The lidar data can be accessed at www.unavco.org. We would like to thank Dimitri Lague, Steve DeLong, Dennis Staley, Jon Pelletier, John Buffington, and an anonymous reviewer whose comments greatly improved this paper. Any use of trade, product, or firm names is for descriptive purposes only and does not imply endorsement by the U.S. Government.

References

Benavides-Solorio, J., and L. MacDonald (2001), Post-fire runoff and erosion from simulated rainfall on small plots, Colorado Front Range, *Hydrol. Process.*, *15*(15), 2931–2952.

Benavides-Solorio, J., and L. H. MacDonald (2005), Measurement and prediction of post-fire erosion at the hillslope scale, Colorado Front Range, *Int. J. Wildland Fire*, *14*(4), 457–474.

Brasington, J., B. Rumsby, and R. McVey (2000), Monitoring and modelling morphological change in a braided gravel-bed river using high resolution GPS-based survey, *Earth Surf. Processes Landforms*, *25*(9), 973–990.

Busse, M. D., C. J. Shestak, K. R. Hubbert, and E. E. Knapp (2010), Soil physical properties regulate lethal heating during burning of woody residues, *Soil Sci. Soc. Am. J.*, *74*(3), 947–955.

Cannon, S., J. Gartner, C. Parrett, and M. Parise (2003), Wildfire-related debris-flow generation through episodic progressive sediment-bulking processes, western USA, in *Debris-Flow Hazards Mitigation: Mechanics, Prediction, and Assessment, Proceedings of the Third International Conference on Debris-flow Hazards Mitigation*, pp. 71–82, Millpress, Rotterdam, Netherlands.

Chief, K., M. H. Young, and D. S. Shafer (2012), Changes in soil structure and hydraulic properties in a wooded-shrubland ecosystem following a prescribed fire, *Soil Sci. Soc. Am. J.*, *76*(6), 1965–1977.

Collins, B., S. Corbett, H. Fairley, D. Minasian, R. Kayen, T. Dealy, and D. Bedford (2012), Topographic change detection at select archeological sites in Grand Canyon National Park, Arizona, 2007–2010, *U.S. Geol. Surv. Sci. Invest. Rep. 2012–5133,* United States Geological Survey, Reston, Va.

Collins, B. D., and N. Sitar (2008), Processes of coastal bluff erosion in weakly lithified sands, Pacifica, California, USA, *Geomorphology*, *97*(3), 483–501.

Day, S. S., K. B. Gran, P. Belmont, and T. Wawrzyniec (2012), Measuring bluff erosion part 1: Terrestrial laser scanning methods for change detection, *Earth Surf. Process. Landforms*, *38*, 1055–1067.

DeBano, L. F. (2000), The role of fire and soil heating on water repellency in wildland environments: A review, *J. Hydrol.*, *231*, 195–206.

DeLong, S. B., W. Henderson, and A. Youberg (2012), Post wildfire landscape change in a small headwater catchment from terrestrial LiDAR, paper presented at Southwest Wildfire Hydrology and Hazards Workshop: Conference Proceedings, Oracle, Ariz., 3rd–5th April.

DiBiase, R. A., and M. P. Lamb (2013), Vegetation and wildfire controls on sediment yield in bedrock landscapes, *Geophys. Res. Lett.*, *40*(6), 1093–1097.

Dietrich, W. E., C. J. Wilson, D. R. Montgomery, and J. McKean (1993), Analysis of erosion thresholds, channel networks, and landscape morphology using a digital terrain model, *J. Geol.*, *101*, 259–278.

Doerr, S., R. Shakesby, and R. Walsh (2000), Soil water repellency: Its causes, characteristics and hydro-geomorphological significance, *Earth Sci. Rev.*, *51*(1), 33–65.

Ebel, B., J. Moody, and D. Martin (2012a), Hydrologic conditions controlling runoff generation immediately after wildfire, *Water Resour. Res.*, *48*, W03529, doi:10.1029/2011WR011470.

Ebel, B., E. Hinckley, and D. Martin (2012b), Soil-water dynamics and unsaturated storage during snowmelt following wildfire, *Hydrol. Earth Syst. Sci.*, *16*(5), 1401–1417, doi:10.5194/hess-16-1401-2012.

Gabet, E. (2003a), Post-fire thin debris flows: Sediment transport and numerical modelling, *Earth Surf. Processes Landforms*, *28*, 1341–1348.

Gabet, E., and T. Dunne (2003), Sediment detachment by rain power, *Water Resour. Res.*, *39*(1), 1002, doi:10.1029/2001WR000656.

Gabet, E., and S. Mudd (2006), The mobilization of debris flows from shallow landslides, *Geomorphology*, *74*, 207–218.

Gabet, E. J. (2003b), Sediment transport by dry ravel, *J. Geophys. Res.*, *108*(B1), 2049, doi:10.1029/2001JB001686.

Gupta, V., K. J. Reinke, S. D. Jones, L. Wallace, and L. Holden (2015), Assessing metrics for estimating fire induced change in the forest understorey structure using terrestrial laser scanning, *Remote Sens.*, *7*(6), 8180–8201.

Hengl, T. (2006), Finding the right pixel size, *Comput. Geosci.*, *32*(9), 1283–1298.

Hodgson, M. E., and P. Bresnahan (2004), Accuracy of airborne LiDAR-derived elevation: Empirical assessment and error budget, *Photogram. Eng. Remote Sens.*, *70*(3), 331–340.
Howard, A., and G. Kerby (1983), Channel changes in badlands, *Bull. Geol. Soc. Am.*, *94*(6), 739–752.
Hungerford, R. D., M. G. Harrington, W. H. Frandsen, K. C. Ryan, and G. J. Niehoff (1991), Influence of fire on factors that affect site productivity, in *Proceedings Management and Productivity of Western-Montane Forest Soils*, edited by A. E. Harvey and L. F. Neuenschwander, pp. 32–50, General Technical Report INT-280, U.S. Department of Agriculture, Forest Service, Intermountain Research Station, Utah.
Imeson, A., J. Verstraten, E. Van Mulligen, and J. Sevink (1992), The effects of fire and water repellency on infiltration and runoff under Mediterranean type forest, *Catena*, *19*(3), 345–361.
Istanbulluoglu, E., D. G. Tarboton, R. T. Pack, and C. Luce (2003), A sediment transport model for incision of gullies on steep topography, *Water Resour. Res.*, *39*(4), 1103, doi:10.1029/2002WR001467.
Istanbulluoglu, E., D. G. Tarboton, R. T. Pack, and C. H. Luce (2004), Modeling of the interactions between forest vegetation, disturbances, and sediment yields, *J. Geophys. Res.*, *109*, F01009, doi:10.1029/2003JF000041.
Jackson, M., and J. Roering (2009), Post-fire geomorphic response in steep, forested landscapes: Oregon Coast Range, USA, *Quat. Sci. Rev.*, *28*, 1131–1146.
Lague, D., N. Brodu, and J. Leroux (2013), Accurate 3D comparison of complex topography with terrestrial laser scanner: Application to the Rangitikei canyon (NZ), *ISPRS J. Photogramm. Remote Sens.*, *82*, 10–26, doi:10.1016/j.isprsjprs.2013.04.009.
Lane, S. N., R. M. Westaway, and D. Murray Hicks (2003), Estimation of erosion and deposition volumes in a large, gravel-bed, braided river using synoptic remote sensing, *Earth Surf. Processes Landforms*, *28*(3), 249–271.
Milan, D., G. Heritage, A. Large, and I. Fuller (2011), Filtering spatial error from DEMs: Implications for morphological change estimation, *Geomorphology*, *125*(1), 160–171.
Montgomery, D. R., and J. M. Buffington (1997), Channel-reach morphology in mountain drainage basins, *Geol. Soc. Am. Bull.*, *109*(5), 596–611.
Moody, J. A., and D. A. Martin (2001a), Initial hydrologic and geomorphic response following a wildfire in the Colorado Front Range, *Earth Surf. Processes Landforms*, *26*, 1049–1070.
Moody, J. A., and D. A. Martin (2001b), Post-fire, rainfall intensity-peak discharge relations for three mountainous watersheds in the western USA, *Hydrol. Process.*, *15*(15), 2981–2993.
Moody, J., and P. Nyman (2013), Variations in soil detachment rates after wildfire as a function of soil depth, flow properties, and root properties, *Sci. Invest. Rep. 2012-5233*, U.S. Geological Survey.
Moody, J., and B. Ebel (2012), Hyper-dry conditions provide new insights into the cause of extreme floods after wildfire, *Catena*, *93*, 58–63.
Moody, J. A., and B. A. Ebel (2013), Infiltration and runoff generation processes in fire-affected soils, *Hydrol. Process.*, *28*, 3432–3453, doi:10.1002/hyp.9857.
Moody, J. A., J. D. Smith, and B. Ragan (2005), Critical shear stress for erosion of cohesive soils subjected to temperatures typical of wildfires, *J. Geophys. Res.*, *110*, F01004, doi:10.1029/2004JF000141.
Moody, J. A., D. A. Martin, and S. H. Cannon (2008), post-wildfire erosion response in two geologic terrains in the western USA, *Geomorphology*, *95*(3), 103–118.
Moreland, D. C., and R. E. Moreland (1975), *Soil Survey of Boulder County Area, Colorado*, Natural Resources Conservation Service, United States Department of Agriculture, Washington, D. C.
Moss, A. (1988), Effects of flow velocity variation on rain driven transportation and the role of rain impact in the movement of solids, *Soil Res.*, *26*(3), 443–450.
Moss, A., P. Walker, and J. Hutka (1979), Raindrop-stimulated transportation in shallow water flows: An experimental study, *Sediment. Geol.*, *22*(3), 165–184.
Nyman, P., G. Sheridan, H. Smith, and P. Lane (2011), Evidence of debris flow occurrence after wildfire in upland catchments of south-east Australia, *Geomorphology*, *125*, 383–401.
Orem, C. A., and J. D. Pelletier (2015), Quantifying the time scale of elevated geomorphic response following wildfires using multi-temporal LiDAR data: An example from the Las Conchas fire, Jemez Mountains, New Mexico, *Geomorphology*, *232*, 224–238.
Owens, P. N., W. H. Blake, T. R. Giles, and N. D. Williams (2012), Determining the effects of wildfire on sediment sources using 137Cs and unsupported 210Pb: The role of landscape disturbances and driving forces, *J. Soils Sediments*, *12*(6), 982–994.
Pelletier, J. D., and C. A. Orem (2014), How do sediment yields from post-wildfire debris-laden flows depend on terrain slope, soil burn severity class, and drainage basin area? Insights from airborne-LiDAR change detection, *Earth Surf. Process. Landforms*, *39*(13), 1822–1832.
Proffitt, A., C. Rose, and P. Hairsine (1991), Rainfall detachment and deposition: Experiments with low slopes and significant water depths, *Soil Sci. Soc. Am. J.*, *55*(2), 325–332.
Riegl (2012), 3D terrestrial laser scanner with online waveform processing, *Tech. Rep.*, Riegl Laser Measurement Systems, Horn, Austria.
Rieke-Zapp, D., J. Poesen, and M. Nearing (2007), Effects of rock fragments incorporated in the soil matrix on concentrated flow hydraulics and erosion, *Earth Surf. Process. Landforms*, *32*(7), 1063–1076.
Robichaud, P., and R. Hungerford (2000), Water repellency by laboratory burning of four northern Rocky Mountain forest soils, *J. Hydrol.*, *231*, 207–219.
Robichaud, P., J. Wagenbrenner, and R. Brown (2010), Rill erosion in natural and disturbed forests: 1. Measurements, *Water Resour. Res.*, *46*, W10506, doi:10.1029/2009WR008314.
Rubio, J. L., J. Forteza, V. Andreu, and R. Cerni (1997), Soil profile characteristics influencing runoff and soil erosion after forest fire: A case study (Valencia, Spain), *Soil Technol.*, *11*(1), 67–78.
Sanford, L. P., and J. P.-Y. Maa (2001), A unified erosion formulation for fine sediments, *Mar. Geol.*, *179*(1), 9–23.
Sankey, J. B., J. U. Eitel, N. F. Glenn, M. J. Germino, and L. A. Vierling (2011), Quantifying relationships of burning, roughness, and potential dust emission with laser altimetry of soil surfaces at submeter scales, *Geomorphology*, *135*(1), 181–190.
Schmidt, K. M., M. N. Hanshaw, J. F. Howle, J. W. Kean, D. M. Staley, J. D. Stock, and G. W. Bawden (2011), Hydrologic conditions and terrestrial laser scanning of post-fire debris flows in the San Gabriel Mountains, CA, USA, edited by R. Genevois, D. L. Hamilton, and A. Prestininzi, pp. 583–593, Italian Journal of Engineering Geology and Environment — Book, Casa Editrice Universita La Sapienza, Rome.
Shakesby, R., and S. Doerr (2006), Wildfire as a hydrological and geomorphological agent, *Earth Sci. Rev.*, *74*(3), 269–307.
Shakesby, R. A., C. Coelho, A. Ferreira, J. Terry, and R. Walsh (1993), Wildfire impacts on soil erosion and hydrology in wet Mediterranean forest, Portugal, *Int. J. Wildland Fire*, *3*(2), 95–110.
Sheridan, G., P. Lane, and P. Noske (2007), Quantification of hillslope runoff and erosion processes before and after wildfire in a wet Eucalyptus forest, *J. Hydrol.*, *343*(1–2), 12–28.

Sinclair, J., and E. Hamilton (1955), Streamflow reactions to a fire-damaged watershed, in *Proceedings Hydraulic Division*, American Society Of Civil Engineers, 81.

Smith, H. G., G. J. Sheridan, P. N. Lane, P. J. Noske, and H. Heijnis (2011), Changes to sediment sources following wildfire in a forested upland catchment, southeastern Australia, *Hydrol. Process.*, *25*(18), 2878–2889.

Soulard, C. E., T. C. Esque, D. R. Bedford, and S. Bond (2013), The role of fire on soil mounds and surface roughness in the Mojave Desert, *Earth Surf. Process. Landforms*, *38*(2), 111–121.

Staley, D. M., T. A. Wasklewicz, and J. W. Kean (2014), Characterizing the primary material sources and dominant erosional processes for post-fire debris-flow initiation in a headwater basin using multi-temporal terrestrial laser scanning data, *Geomorphology*, *214*, 324–338.

Stoof, C. R., J. G. Wesseling, and C. J. Ritsema (2010), Effects of fire and ash on soil water retention, *Geoderma*, *159*(3), 276–285.

Tarboton, D. G. (1997), A new method for the determination of flow directions and upslope areas in grid digital elevation models, *Water Resour. Res.*, *33*(2), 309–319.

Terrasolid Software (2011), Terrascan, Terrasolid, Helsinki. [Available from http://www.terrasolid.com.]

Wheaton, J. M. (2008), Uncertainty in morphological sediment budgeting of rivers, PhD thesis, Univ. of Southampton.

Wheaton, J. M. (2014), *Geomorphic Change Detection Tool*, Utah State University. [Available from http://gcd.joewheaton.org/.]

Wheaton, J. M., J. Brasington, S. E. Darby, and D. A. Sear (2010), Accounting for uncertainty in DEMs from repeat topographic surveys: Improved sediment budgets, *Earth Surf. Process. Landforms*, *35*(2), 136–156.

Wilkinson, S., P. Wallbrink, G. Hancock, W. Blake, R. Shakesby, and S. Doerr (2009), Fallout radionuclide tracers identify a switch in sediment sources and transport-limited sediment yield following wildfire in a Eucalypt forest, *Geomorphology*, *110*(3), 140–151.

Wohl, E. (2013), Migration of channel heads following wildfire in the Colorado Front Range, USA, *Earth Surf. Process. Landforms*, *38*(9), 1049–1053.